Coulomb Explosion Dynamics of Chlorocarbonylsulfenyl Chloride

Graham A. Cooper[1], S. Tahereh Alavi[1], Wen Li[2], Suk-Kyoung Lee[2], and Arthur G. Suits[1,]*

[1]Department of Chemistry, University of Missouri, Columbia, MO, USA

[2]Department of Chemistry, Wayne State University, Detroit, MI, USA

ABSTRACT

The Coulomb explosion dynamics following strong field ionization of chlorocarbonylsulfenyl chloride were studied using multimass coincidence detection and covariance imaging analysis, supported by density functional theory calculations. These results show evidence of multiple dissociation channels from various charge states. Double ionization to low-lying electronic states leads to a dominant C–S cleavage channel, while higher states can alternatively correlate to loss of Cl^+. Triple ionization leads to a double dissociation channel, the observation of which is confirmed via three-body covariance analysis, while further ionization leads primarily to atomic or diatomic fragments whose relative momenta depend strongly on the starting structure of the molecule.

1. Introduction

The ability of Coulomb Explosion Imaging (CEI) to directly probe the structure of a molecule following multiple ionization by ultrafast methods has led to significant interest in both the technique itself and its application in time-resolved experiments.[1–6] Developments over the last decade in time-dependent imaging sensors such as the PImMS sensor have simplified the acquisition of multimass imaging data required for covariance analysis and structural determination.[7–13] However, it has been shown that multimass detection can be accomplished using fast cameras and digitizers in a coincidence detection setup, with advantages in both temporal and velocity resolution.[14,15] In this work, we demonstrate that the 3D (time and position) coincidence detection approach is capable of successful CEI experiments for structural determination, holding promise for future pump-probe studies.

Chlorocarbonylsulfenyl chloride (ClC(O)SCl; hereafter CCSC) is a synthetic reagent used primarily to create cyclic thioesters or for carbonyl coupling.[16–18] The structural and spectroscopic parameters of CCSC and similar compounds, and their photochemical behavior, have been studied multiple times over the course of several decades.[19–28] These have shown that the dominant conformer of CCSC is planar with the C=O and S–Cl bonds in a *syn* orientation,[19,20,24] and that it exhibits a rich photochemistry when exposed to ultraviolet irradiation.[25,27]

Two studies have also previously examined the dynamics of ionized CCSC produced by valence and core synchrotron ionization.[26,28] These showed that while $CCSC^+$ undergoes C–S, S–Cl or C–Cl bond rupture processes to produce molecular fragments,[28] removal of further electrons opens up a wide range of other fragmentation pathways with increasing degrees of atomization as the excitation energy increased.[26] These pathways from multiply ionized CCSC were identified

through ion-ion coincidence measurements, including several involving Coulomb explosion (CE), where multiple cationic fragments are produced and subsequently accelerated apart under the effect of electrostatic repulsion.

In this study, we examine the energetics and dynamics of $CCSC^{n+}$ ($n \geq 2$) produced by strong field ionization using multimass coincidence imaging. With the use of covariance image analysis techniques, we are able to observe both the energy and relative orientation of multiple products from the same fragmentation, and these data are used to reveal details about Coulomb explosions occurring in these parent cations.

2. Methods

2.1 Experimental Methods

The experiments in this study were conducted using a velocity map imaging (VMI) apparatus adapted for multimass imaging of Coulomb explosions, shown in Figure 1. CCSC (Sigma-Aldrich, 96%) was seeded in He (Airgas, Grade 4.5) by passing the carrier gas through a bubbler containing a degassed liquid sample. This gas mixture was introduced to the chamber using a piezoelectric disc valve[29] opened for 30 µs per pulse (controlled using a DEI PVX-4150 Pulse Generator with timing from a BNC Model 577 Pulse Generator), with the backing gas at a pressure of ~500 Torr. This gas jet entered the source chamber (at a resting pressure of ~10^{-7} Torr) and passed through a 0.2 mm skimmer into the main chamber (~10^{-9} Torr). Both chambers were pumped using turbomolecular pumps and the pressure in the main chamber was further reduced using a liquid nitrogen cold finger.
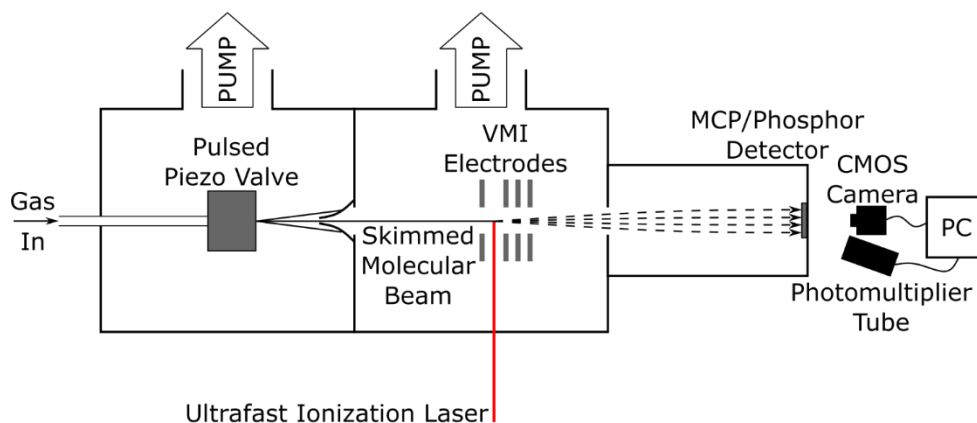
Figure 1 – Schematic diagram of experimental apparatus used in this study.

This molecular beam was intersected in the interaction region of a VMI electrode array by the ionization laser pulse. This was produced using a KMLabs Wyvern-1000 Ti:Sapphire laser, which outputs 800 nm pulses with a 100 fs duration at ~2 mJ/pulse at a 1 kHz repetition rate, although the experiment is performed at a ~250 Hz rate, limited by the speed of the PC collecting the data through the method described below. The power of these pulses was reduced using a combination of beamsplitters and neutral density filters, before being focused into the vacuum chamber using a 25 cm lens to produce a strong field with intensities varying in the $7 - 20 \times 10^{13}$ W/cm^2 range.

This strong field ionized the target molecules, producing ions which were focused onto the detector using VMI electrodes in a DC slicing configuration.[30] A twin microchannel plate (MCP) detector with a phosphor screen was used, with the detector gated to selectively detect the desired fragments (using another DEI PVX-4150 pulser), and the screen was observed using both a CMOS camera (Basler acA720-520um) and a photomultiplier tube (PMT) connected to a digitizer (NI PCI-5114) which were controlled using the same computer. Images were acquired at a resolution of 480×480 pixels, and the camera and digitizer are capable of 260×260 pixel resolution at 1 kHz. While

images of a single fragment can be collected by gating the detector over the corresponding time delay, this setup also allowed for the use of the 3D coincidence multimass imaging technique previously described by Lee et al.[14]

In this approach, each camera frame is analyzed to find ion events above a specified intensity threshold, the locations of which are centroided and then recorded, along with the event intensities, for each experimental repetition. Simultaneously, the time-of-flight (ToF) spectrum is recorded for each laser shot and subsequently run through a peak detection program to create a list of peak locations and amplitudes for each spectrum. The camera and PMT lists are then compared on a shot-by-shot basis, and where the number of events in each list is identical, they are then matched using their camera intensities and spectral amplitudes, assuming that the magnitude of the signal observed in each case will be related. The matching is taken to be successful when the intensities and amplitudes of the matched events show a strong correlation. In this way, a list of ion events with both time and position data can be created, allowing for multiple fragments to be observed simultaneously by determining which fragment is responsible for each event detected by the camera.

Images were calibrated using the known Coulomb Explosion behavior of CH_3I under similar conditions, such that radial spectra could be converted to velocity distributions. These were subsequently transformed to fragment translational energy (fE_T) space, or, in the case of two-body fragmentations, to total translational energy (E_T) space using conservation of momentum. Throughout this work, $p(fE_T)$ and $p(E_T)$ denote the fragment and total translational energy distributions respectively.

2.2 Computational Methods

Supporting calculations were performed at a Density Functional Theory (DFT)[31,32] level using the ωB97X-D functional[33] and Dunning's aug-cc-pVTZ basis set.[34–36] These consisted of optimizing the ground state geometry of the neutral parent molecule and relevant fragments, and producing scans of electronic energy along various bond-stretching coordinates. These scans were also conducted on excited electronic states using time dependent (TD) DFT.[37–43] All calculations were performed using the Gaussian 09 software package.[44]

3 Results and Discussion

Figure 2 shows the distribution of fragments resulting from strong field ionization of CCSC at $\sim 7 \times 10^{13}$ W/cm^2, illustrating that the most intense product peaks (CO+, S+, and Cl+) are those
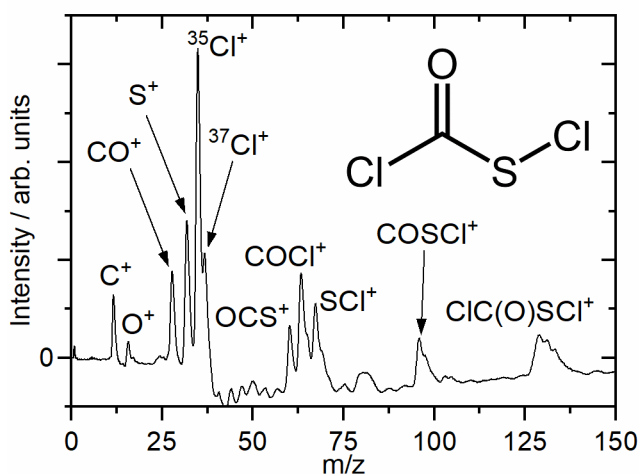

Figure 2 – Time-of-flight mass spectrum resulting from strong field ionization and fragmentation of chlorocarbonylsulfenyl chloride (structure shown in inset). Spectrum is Jacobian-corrected and background-subtracted to show only intensity arising from species in the molecular beam. Inset: skeletal structure of the CCSC parent molecule

which would arise from cleavage of all the single bonds in the molecule (although other processes likely also contribute to their occurrence), while larger fragments are present in lower abundance. The intensity of the parent monocation peak is lower than expected, and peaks from $CCSC^{n+}$ ($n \geq 2$) are absent, due to reduced sensitivity in the center of the detector used, resulting in preferential detection of ions with off-axis momentum.

Images were recorded while gating the MCP voltages over each fragment ion separately; these are shown in Figure S1. The dark spot observed in each image arises from the region of reduced sensitivity mentioned above, arising from damage incurred prior to this project. Due to this damage, the experiment was subsequently repeated with a newer detector without this spot, and the corresponding images can be seen in Figure S2. These show similar results, although the images are at a different size and lower resolution (392×392) due to the smaller size of the replacement detector.

The major difference between the two sets of images is increased intensity in the area previously affected by the damaged spot, as expected. This intensity is primarily the result of dissociative ionization from $CCSC^+$, and would also be where $CCSC^{n+}$ and other non-fragment ions would primarily be observed at the corresponding delay times. Due to this damage, it is not possible in this study to comment on these low translational energy processes. However, the processes of interest for Coulomb explosion, arising from multiply charged ions, tend to occur with higher off-axis velocities and these result in features less affected by the damaged spot.

When performing multimass coincidence experiments, it is impossible to resolve the positions of multiple ions observed too close temporally, which produce a single peak in the ToF spectrum but more than one spot on the camera, which cannot then be correctly matched. It was found that the

data recorded with the newer detector, with the ability to observe extra events which would previously have fallen within the damaged area, had an increased propensity for this to occur, and steps needed to be taken to reduce the number of ions observed. These included manually obscuring the center of the image in order to block out ions with low off-axis momenta, corresponding to non-CE dynamics, such that ions from the processes of interest with similar ToFs could be successfully observed. Given these issues, as well as the reduced detector area and resulting decrease in camera image resolutions, it was found that the data collected with the damaged detector were superior for coincidence detection. While the damaged spot appears unsightly in Figure S1, the features of interest are not obscured, and the reduced sensitivity in this area was in fact a benefit, and thus all subsequent data in this publication are those acquired with the older, larger detector.

Three fragments show clear rings in the images in Figure S1, most prominently $COCl^+$ and SCl^+. The central slices of these images were reconstructed using Finite Slice Analysis (FinA),[45,46] and the total translational energy spectra are shown in Figure 3.

The intensity close to the center of the images (obscured or blocked by the less sensitive area of the detector) results from dissociative ionization processes via $CCSC^+$. The rings in both images are momentum matched and correspond to the same peak E_T value of 6.1 eV when the features are assumed to arise from two-body fragmentation of $CCSC^{n+}$, suggesting they arise from the same process, i.e.
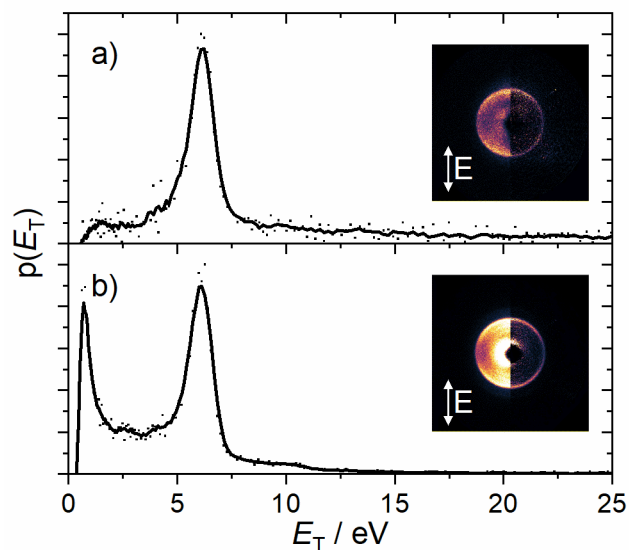
$$ClC(O)SCl^{2+} \rightarrow COCl^+ + SCl^+ \qquad (1)$$

Figure 3 – Translational energy spectra from FinA-reconstructed images of (a) SCl^+ and (b) $COCl^+$. E_T values were calculated using momentum conservation assuming $COCl^{0/+}$ and $SCl^{0/+}$ co-fragments respectively. The dots indicate the raw values, with the lines representing a 5-point running average. Inset: VMI images corresponding to the displayed spectra, with the raw image on the left and the reconstructed central slice on the right; the arrows indicate the direction of the laser polarization.

The rings shown in Figure 3 show significant anisotropy, with β_2 values from the FinA reconstruction of $0.6 - 0.8$. While the CO^+, S^+, and Cl^+ images (seen in Figure S1) show more diffuse intensity without clear rings, they likewise show anisotropic distributions, perpendicular to the polarization vector of the laser field in the first two cases and parallel in the latter. These features arise from the well-studied alignment effects in strong field ionization, where molecules are preferentially ionized when the molecular axis is oriented parallel to the laser polarization vector (geometric alignment), or where molecules are rotated by the field such that the axis points in that direction (dynamic alignment).[47] Given the duration of the pulse, it is likely that there is a significant dynamic alignment effect, but the exact nature of the observed alignment is not certain.

The observed images indicate that the molecule is preferentially ionized with the axis along the molecular backbone (between the terminal Cl atoms) parallel to the polarization of the laser field. For processes (1), this results in the product ions travelling primarily parallel to the polarization vector. For the Coulomb explosions of more highly charged $CCSC^{n+}$ which substantially contribute to the smaller fragment images (as examined below), the observed anisotropic distributions arise from the Cl^+ ions being propelled along the molecular axis while CO^+ and S^+ are pushed to the sides by electrostatic repulsion.

To confirm the assignment of process (1), the multimass imaging capabilities of the experiment were utilized to simultaneously observe fragments in the mass spectrum (seen in Figure 2) between CO^+ and $COSCl^+$, inclusive. From these, the covariance maps for the relationship between pairs of fragments were calculated using the process described by Slater et al.[7,8]

The covariance maps are calculated between pairs of 'reference' and 'plotted' ions, and show where the plotted ions are more likely to be seen in a frame in which the reference ions are oriented along a specified axis from the center (here always vertically upwards). The map for covariance of $COCl^+$ referenced to SCl^+ was calculated and is shown in Figure 4(a). A very sharp feature centered around 180° is observed in both this map and the reverse case, indicating that there exists a two-body fragmentation producing these ions. Given that these features are observed at the same radii as the rings shown in Figure 3, this confirms that process (1), C–S bond cleavage from $CCSC^{2+}$, is responsible for these rings. Covariance of Cl^+ referenced to $COCl^+$ is shown in Fig. 4b to facilitate comparison, but this will be discussed in the three-body section below.
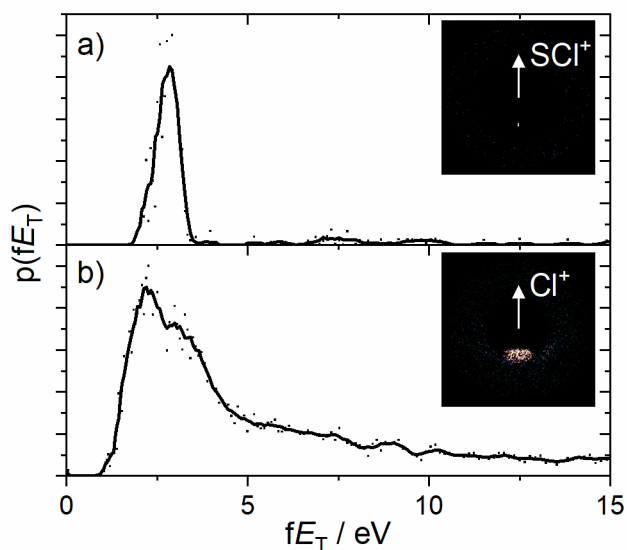

Figure 4 – Fragment translational energy distributions from covariance maps of $COCl^+$ referenced to (a) SCl^+ (within angles of $176 - 183°$ to the reference ion vector) and (b) Cl^+ (at $144 - 216°$ angles). Points represent raw data while the lines indicate the five-point running average. Insets: the covariance maps from which the spectra are extracted, with adjacent pixel smoothing and arrows showing the orientation vector of the reference ion.

Computational scans were conducted along $R_{C–S}$ for $CCSC^{2+}$ in the lowest-lying singlet and triplet states, as shown in Figure 5 (additional curves are shown in Figure S3 for further excited states). These illustrate that the two lowest energy singlet states are dissociative along this coordinate, with little or no barrier to fragmentation. The difference in energy between the parent dication states in the neutral ground state equilibrium geometry and the relaxed products of process (1) in the lowest spin-allowed electronic states are 6.6 or 6.3 eV from the triplet or singlet states respectively, which agrees well with the E_T value of 6.1 eV observed from the images in Figure 3. These calculations thus suggest that these rings arise from C–S cleavage after ionization to ground or low-lying states of $CCSC^{2+}$, driven by Coulomb repulsion between the product fragments. A simple model treating
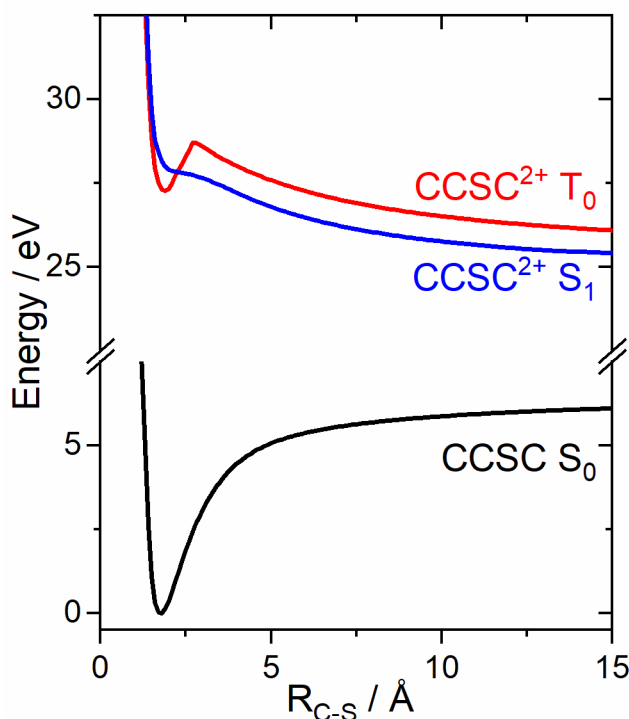

Figure 5 – Potential energy curves for CCSC along the C–S elongation coordinate in the neutral ground state (black), triplet ground state of $CCSC^{2+}$ (red), and lowest-lying singlet state of $CCSC^{2+}$ (blue), calculated at the ωB97X-D/aug-cc-pVTZ level. All other coordinates were fixed at their values from the ground state neutral equilibrium geometry.

the product ions as simple point charges moving only under electrostatic repulsion would predict $E_T = 7.8$ eV, significantly higher than both the DFT treatment and the experimental value. This may arise from multiple contributing factors: firstly, the bonding forces in the dication may have a non-negligible impact, requiring additional energy to overcome. However, it is also possible that the difference may arise from distortion of the molecule during the process of ionization; previous studies have observed experimental energy releases substantially lower than those expected from pure Coulombic repulsion, potentially attributed to stretching during ionization.[48,49] The difference is less significant than that observed in those cases, potentially due to the shorter laser pulses and thus reduced time for deformation. This bond stretching can be driven or selected for by the nature of the ionization process, where increasing bond length can decrease the ionization threshold.[50,51]

The third image in Figure S1 which shows a clear ring is that appearing at $m/z = 95$, corresponding to either Cl–C(O)–S$^+$ or C(O)–S–Cl$^+$, which arises from loss of a single Cl atom at either end of the molecule. However, the two potential fragments produced by C–Cl and S–Cl cleavage cannot be distinguished by time-of-flight and thus either or both may contribute to the image. This image, and the corresponding E_T spectrum, is shown in Figure 6, where the central intensity again arises from dissociative ionization via CCSC$^+$, and the faster ring at 5.1 eV seems likely to arise from Coulomb-explosion loss of Cl$^+$ from the dication, i.e.
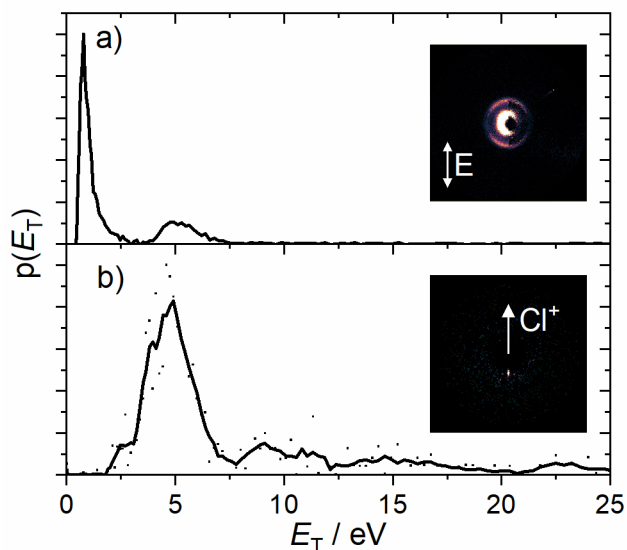

Figure 6 – Translational energy spectra (assuming a Cl$^{0/+}$ co-fragment) from (a) the FinA-reconstructed image of COSCl$^+$, shown in the inset (with the raw image on the left and the reconstruction on the right; the arrow indicates the laser polarization orientation) and (b) the covariance map of COSCl$^+$ referenced to Cl$^+$, gated over angles $177 - 183°$ to the reference vector, shown in the inset (with adjacent pixel smoothing; the arrow indicates the direction of the reference ion). Points indicate raw data, with a five-point weighted average shown by the line.

$$ClC(O)SCl^{2+} \rightarrow COSCl^+ + Cl^+ \qquad (2)$$

This ring shows similar anisotropy to those in Figure 3, with a β_2 value of 1.1, for the same dynamic alignment reasons. A similar covariance map to that in Figure 4(a), showing a sharp feature centered around 180°, was found for $COSCl^+$ referenced to Cl^+, as shown in Figure 6(b). The radial spectrum shows that this feature peaks at similar radii to the ring in the images shown in Figure 6(a), confirming that process (2), the loss of Cl^+ from $CCSC^{2+}$, gives rise to this feature. The reverse map does not show any significant structure, suggesting the fraction of Cl^+ arising from this channel is a small fraction of the total, such that it is not resolved in the calculated map. A comparison of the intensity of the number of Cl^+ ions observed in the image in Figure S1 to the number of counts in the ring in Figure 6(a) suggests that this channel accounts for less than 0.5% of Cl^+ ions observed, supporting this assertion.

It remains ambiguous which Cl atom is lost in this process, and similar potential energy curves to those shown in Figure 5 were calculated along $R_{C–Cl}$ and $R_{S–Cl}$, as shown in Figure S4. The computed curves show that relative to the triplet ground state of $CCSC^{2+}$ at the starting geometry, the relaxed products of C–Cl and S–Cl cleavage are 2.9 and 1.2 eV lower in energy, respectively, with corresponding barriers to dissociation of 1.5 and 2.8 eV (the maximum energy releases from the lowest singlet state are reduced to 1.2 and 0.0 eV). The low-lying states studied via TD-DFT also show barriers along these coordinates. The fact that the translational energy measured for the process is noticeably higher, at 5.1 eV, and that the dication ground state is bound with respect to Cl-loss but not C–S cleavage, suggests that process (2) instead results from ionization to an excited state which preferentially loses a Cl^+ ion, rather than the singlet ground state which is likely to

promptly follow the pathway of process (1). While C–Cl cleavage results in the more stable product ion, further computational work at a higher level of theory beyond the scope of this work would be required to identify the excited state which best explains the observed behavior in order to determine conclusively which Cl atom is lost.

In order to identify further fragmentation pathways of $CCSC^{2+}$, covariance maps were calculated between other pairs of ions. The map of $COCl^+$ referenced to Cl^+ shows a particularly significant feature, centered around $180°$ but broader than those observed for the two-body dissociations described previously. This is accounted for by the additional momentum of the unobserved third fragment. This map, and the corresponding fragment translational energy spectrum, are compared in Figure 4 to the map and fE_T spectrum from $COCl^+$ referenced to SCl^+ (i.e., resulting from process (1)).

These spectra show that the radial profiles of the two features are similar but distinct; process (1) produces a sharp peak at 3.1 eV, while the spectrum in Figure 4(b) shows a broader feature peaking at 2.4 eV but which is relatively flat in the $2.1 – 3.6$ eV range (the higher background level at higher radii results from a lower signal to noise ratio in this map as it corresponds to a lower proportion of the $COCl^+$ ions). Given the lack of data on the momentum of the third fragment ($S^{0/+}$), it is impossible to convert this to total E_T, but the range of angles observed in the covariance map allow for some limits to be placed on the possible values. The observed feature covers the angles $145 – 180°$, so given this and equations for conservation of momentum, a lower bound can be placed on E_T of $4.1 – 8.4$ eV. Here the lower bound corresponds to the slower $COCl^+$ ions at 2.1 eV with an angle to the reference vector close to $180°$ and the upper bound corresponds to an fE_T of 3.6 eV and angles closer to $145°$.

This lower bound occurs when the angle between the sulfur and chlorine momenta is acute, and the actual total translational energy could be higher. DFT calculations suggest an overall change in energy from the T_0 or S_1 states of $CCSC^{2+}$ of only –0.2 or –1.1 eV for process (3),

$$ClC(O)SCl^{2+} \rightarrow COCl^+ + S + Cl^+ \tag{3}$$
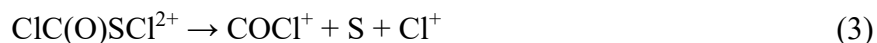
Given the large translational energy observed experimentally, compared to the small energy release for this process, two plausible explanations arise. The first is that strong field ionization accesses one or more excited states of $CCSC^{2+}$ 5 – 10 eV above the dication ground state, similar to but higher in energy than the states responsible for pathway (2), which undergoes dissociation along this pathway; the second involves the removal of an additional electron by the laser field to reach $CCSC^{3+}$, which promptly produces $COCl^+$, S^+, and Cl^+ with a calculated release of 10.8 eV of energy in process (4),

$$ClC(O)SCl^{3+} \rightarrow COCl^+ + S^+ + Cl^+ \tag{4}$$
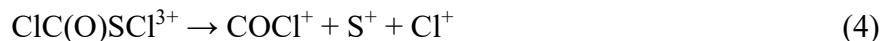
To examine the possibility of the trication assignment, the three-fold covariance analysis described by Pickering et al. was used.[9] This approach yields a map analogous to that in Figure 4(b) with the added constraint that an S^+ ion must also be observed in the same camera frame; the relative orientation of this third ion with respect to the reference can also be constrained.

These maps are shown in Figure 7; note that they are calculated at reduced resolution due to the prohibitive time costs of the calculations at full resolution. Figure 7(d) shows how the map from Figure 4(b) appears at this resolution, and this map bears a significant resemblance to that in Figure 7(b), featuring intensity in the same region shown by the green ellipse. This intensity is also present
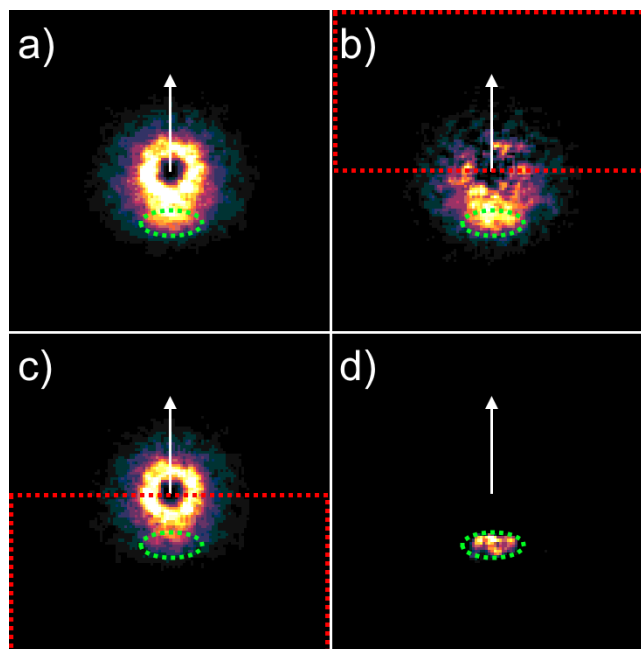
Figure 7 – Covariance maps for $COCl^+$ referenced to Cl^+ (the orientation of which is indicated by the arrows). (a) Three-body map with no constraints on position of the third ion, S^+; (b) & (c) three-body maps with S^+ constrained to the areas within the red boxes; (d) two-body map without any S^+ requirement. The green ellipses indicate the same area in all images and all images use adjacent pixel smoothing.

in panel (a), but is absent in (c). This behavior, with the same feature appearing in the 2- and 3-body maps, but being dependent on the constraints placed on the third ion, is in keeping with that expected for a three body dissociation featuring all three ions, strongly suggesting that process (4) is responsible for the feature observed in the two- and three-fold covariance maps.

Other anisotropic features were observed in covariance maps calculated between other pairs of fragments, but in most cases the signal-to-noise ratio in these features is not sufficient to enable proper analysis. However, they strongly imply the existence of other potential exit channels from the di- and trication of CCSC. One other map which shows a strong covariance pattern is that of S^+ referenced to Cl^+. This is compared in Figure 8 to the corresponding covariance map when the

intensity of the laser field was raised to 2×10^{14} W/cm^2 in order to increase the average charge state reached by the CCSC molecules. This change resulted in the number of smaller fragment ions (CO$^+$, S$^+$, and Cl$^+$) increasing relative to the larger molecular fragments, and doubly ionized products also being increasingly observed. Multifragment images were recorded over these ions, covering the $16 - 37$ *m/z* range (S^{2+} to ^{37}Cl$^+$). Attempts to include lighter or more highly charged fragments in the gated range were frustrated by light organic ions originating from background contaminants in the chamber.

In Figure 8 it can be seen that in both cases the S^+ is primarily observed to the sides. This is in contrast to the covariance maps for Cl^{2+} reference to Cl^+ recorded under the higher intensity
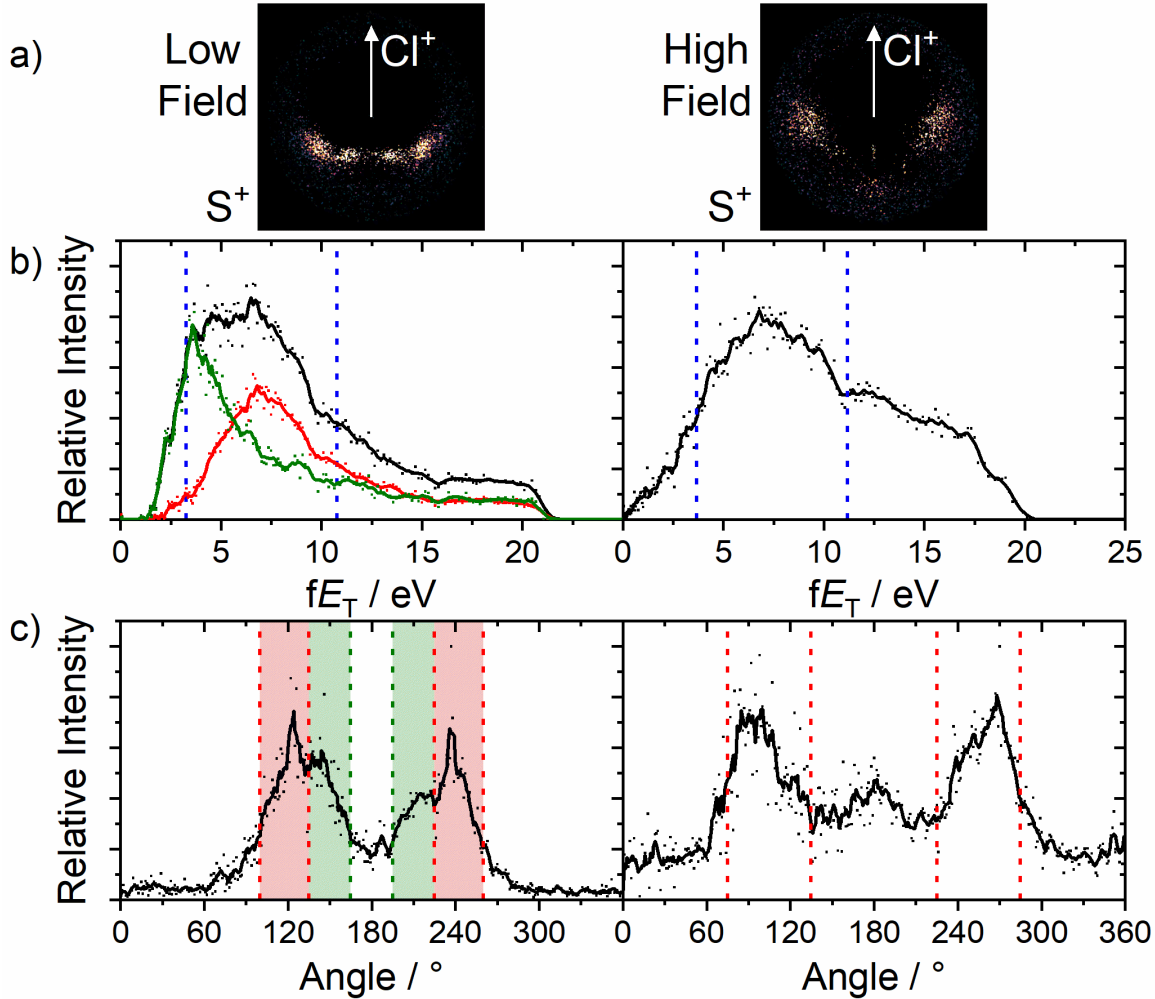

Figure 8 – (a) Covariance maps for S^+ referenced to Cl^+ in weaker (left) and stronger (right) laser fields, with adjacent pixel smoothing and arrows indicating the orientation vector for the reference ions; (b) fE_T distributions corresponding to the above maps within the angular ranges indicated on the lower panels. In the left hand column, the red and green lines corresponds to the ranges highlighted in the bottom panel, with the black trace the total across both ranges; (c) angular distributions for the respective images within the radial ranges indicated in blue on the middle panels. Points represent raw data while the lines are five-point running averages.

conditions, as can be seen in Figure S5. This is as expected based on the starting geometry of the molecule: for $CCSC^{n+}$ ($n \geq 3$), if there are charges localized on both Cl atoms and the S atom (and additionally on the C or O atoms), then the Cl ions will be expelled in opposite directions while the S^+ is 'squeezed' out perpendicularly by the repulsion from the Cl on either side. This link between starting geometry and Coulomb explosion covariance maps is similar to that previously demonstrated on other molecules,[7,8] and is an important step in establishing the viability of Coulomb explosion imaging in this experiment as an instantaneous probe of molecular structure for pump-probe experiments.

The increasing laser field strength changes the shape of the covariance map significantly. In the lower field case, more intensity is seen closer to 180°, and the plots in Figure 8(b) show that these ions are observed with lower translational energy. As the field strength is increased, this intensity diminishes in favor of more ions being observed at more acute angles, and these ions peak closer to 90° than even the peaks within the range highlight in red on the left panel of Figure 8(c). These observations suggest that in the lower field intensity, there is significant contribution from fragmentation of lower charge states of CCSC, where the unobserved Cl atom may be neutral or carrying a low charge, resulting in the angle between Cl^+ and S^+ being closer to 180° and the translational energy being lower. In the high field case, more electrons are removed and the angle gets significantly more acute as the increasing charge on the unobserved Cl fragment increases (for fixed charges on the observed ions in this case). The covariance map on the right of Figure 8 thus shows a 'purer' Coulomb explosion, with fragment ions moving primarily under the effects of Coulomb repulsion and their trajectories closely reflecting the starting geometry of the molecule. Simple Coulomb-only simulations suggest that the fragmentation of $CCSC^{5+}$ to Cl^+,

Cl^{2+}, S^+, and CO^+ might be expected to yield S^+ ions with a translational energy release of ~8 eV and a relative angle to Cl^+ of 90°, in keeping with the results observed here.

Interesting covariance maps are also observed for CO^+ referenced to S^+ or vice versa, as shown in Figure 9. These maps show a sharp feature centered around 180°, similar to those observed from two-body dissociations such as processes (1) and (2). This feature is only observed under the higher laser field intensity used. The most plausible explanation for these features appears to be a two-step fragmentation of $CCSC^{4+}$, where two Cl^+ ions are ejected approximately in concert to leave behind OCS^{2+} with relatively low momentum, which subsequently undergoes explosive
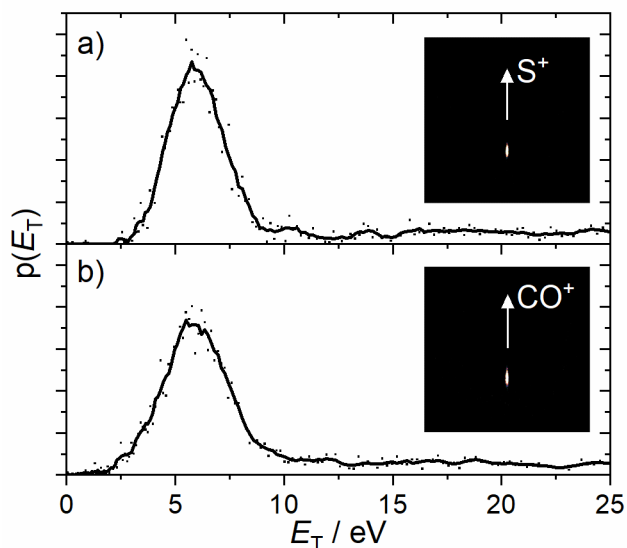

Figure 9 - Translational energy distributions from covariance maps of (a) CO^+ referenced to S^+ and (b) S^+ referenced to CO^+ (both within angles of $170 - 190°$ to the reference ion vector), assuming that the reference ion is the co-fragment for conservation of momentum. Points represent raw data while the lines indicate the five-point running average. Insets: the covariance maps from which the spectra are extracted, with adjacent pixel smoothing and arrows showing the orientation vector of the reference ion.

dissociation to give the observed products. It is also potentially possible, within the duration of the pulses used in this experiment, that the initial loss of $2Cl^+$ occurs from $CCSC^{3+}$, with an additional ionization of OCS^+ triggering the dissociation.

Figure 9 also shows that if the dissociation is treated as a two-body fragmentation of OCS^{2+}, the two features are well momentum-matched, with peaks appearing around 6.0 eV (excluding the additional translational energy of the Cl^{n+} fragments). This matches well to the predicted energy release of 6.2 eV in a Coulomb-only model for the fragmentation of OCS^{2+} (starting from the equilibrium geometry of CCSC without Cl atoms), but is significantly higher than the predicted energy release to optimized products of ca. 3.1 eV in ωB97X-D calculations. This suggests that the observed features can be best explained as arising from a primarily Coulomb-driven process from a high charge state of $CCSC^{n+}$ wherein the Cl^{n+} fragment momenta nearly offset, allowing for two-body-like behavior of the remaining product ions.

4 Conclusions

Chlorocarbonylsulfenyl chloride undergoes multiple ionization and fragmentation processes when exposed to strong laser fields. Following double ionization, the dominant process is C–S cleavage, as the ground electronic state of $CCSC^{2+}$ is dissociative along this coordinate. However, an alternative pathway featuring loss of Cl^+ is also observed, with recorded translational energies indicating that this occurs on excited surfaces exhibiting a barrier to breaking the C–S bond. Further ionization to the trication leads to process such as three-body fragmentation to yield $COCl^+$, S^+, and Cl^+, confirmed using three-body covariance analysis techniques, while removing further electrons leads to higher degrees of atomization where the relative trajectories of the product ions are derived from the parent molecule's starting geometry. These results demonstrate

the ability of the 3D multimass coincidence technique to observe a range of Coulomb explosion dynamics while achieving excellent resolution compared to time-stamped imaging sensors.

ASSOCIATED CONTENT

Supporting Information.

The Supporting information is available free of charge at <journal URL>.

Velocity map images from individual fragments of Coulomb explosion with new and old detectors; calculated potential curves for excited states of $CCSC^{2+}$ along C–S, C–Cl, and S–Cl bond stretching coordinates; and covariance maps for Cl^{2+} and S^+ fragments referenced to Cl^+ following Coulomb explosion in high intensity laser fields (PDF)

AUTHOR INFORMATION

Corresponding Author

*E-mail: suitsa@missouri.edu   Tel: +1 573 882 2976

Author Contributions

The manuscript was written through contributions of all authors. All authors have given approval to the final version of the manuscript.

Notes

Any additional relevant notes should be placed here.

REFERENCES

(1)   Stapelfeldt, H.; Constant, E.; Sakai, H.; Corkum, P. B. Time-Resolved Coulomb Explosion Imaging: A Method to Measure Structure and Dynamics of Molecular Nuclear Wave Packets. *Phys. Rev. A* **1998**, *58* (1), 426–433. https://doi.org/10.1103/PhysRevA.58.426.

(2)   Ellert, Ch.; Stapelfeldt, H.; Constant, E.; Sakai, H.; Wright, J.; Rayner, D. M.; Corkum, P. B. Observing Molecular Dynamics with Timed Coulomb Explosion Imaging. *Philos. Trans. R. Soc. Lond. Ser. Math. Phys. Eng. Sci.* **1998**, *356* (1736), 329–344. https://doi.org/10.1098/rsta.1998.0168.

(3)   Hasegawa, H.; Hishikawa, A.; Yamanouchi, K. Coincidence Imaging of Coulomb Explosion of CS2 in Intense Laser Fields. *Chem. Phys. Lett.* **2001**, *349* (1), 57–63. https://doi.org/10.1016/S0009-2614(01)01087-9.

(4)   Légaré, F.; Lee, K. F.; Litvinyuk, I. V.; Dooley, P. W.; Wesolowski, S. S.; Bunker, P. R.; Dombi, P.; Krausz, F.; Bandrauk, A. D.; Villeneuve, D. M.; Corkum, P. B. Laser Coulomb-Explosion Imaging of Small Molecules. *Phys. Rev. A* **2005**, *71* (1), 013415. https://doi.org/10.1103/PhysRevA.71.013415.

(5)   Gagnon, J.; Lee, K. F.; Rayner, D. M.; Corkum, P. B.; Bhardwaj, V. R. Coincidence Imaging of Polyatomic Molecules via Laser-Induced Coulomb Explosion. *J. Phys. B At. Mol. Opt. Phys.* **2008**, *41* (21), 215104. https://doi.org/10.1088/0953-4075/41/21/215104.

(6)   Corrales, M. E.; Gitzinger, G.; González-Vázquez, J.; Loriot, V.; de Nalda, R.; Bañares, L. Velocity Map Imaging and Theoretical Study of the Coulomb Explosion of CH3I under Intense Femtosecond IR Pulses. *J. Phys. Chem. A* **2012**, *116* (11), 2669–2677. https://doi.org/10.1021/jp207367a.

(7)   Slater, C. S.; Blake, S.; Brouard, M.; Lauer, A.; Vallance, C.; John, J. J.; Turchetta, R.; Nomerotski, A.; Christensen, L.; Nielsen, J. H.; Johansson, M. P.; Stapelfeldt, H. Covariance Imaging Experiments Using a Pixel-Imaging Mass-Spectrometry Camera. *Phys. Rev. A* **2014**, *89* (1), 011401. https://doi.org/10.1103/PhysRevA.89.011401.

(8)   Slater, C. S.; Blake, S.; Brouard, M.; Lauer, A.; Vallance, C.; Bohun, C. S.; Christensen, L.; Nielsen, J. H.; Johansson, M. P.; Stapelfeldt, H. Coulomb-Explosion Imaging Using a Pixel-Imaging Mass-Spectrometry Camera. *Phys. Rev. A* **2015**, *91* (5), 053424. https://doi.org/10.1103/PhysRevA.91.053424.

(9)   Pickering, J. D.; Amini, K.; Brouard, M.; Burt, M.; Bush, I. J.; Christensen, L.; Lauer, A.; Nielsen, J. H.; Slater, C. S.; Stapelfeldt, H. Three-Fold Covariance Imaging of Laser-Induced Coulomb Explosions. *J. Chem. Phys.* **2016**, *144* (16), 161105. https://doi.org/doi:http://dx.doi.org/10.1063/1.4947551.

(10)   Burt, M.; Boll, R.; Lee, J. W. L.; Amini, K.; Köckert, H.; Vallance, C.; Gentleman, A. S.; Mackenzie, S. R.; Bari, S.; Bomme, C.; Düsterer, S.; Erk, B.; Manschwetus, B.; Müller, E.; Rompotis, D.; Savelyev, E.; Schirmel, N.; Techert, S.; Treusch, R.; Küpper, J.; Trippel, S.; Wiese, J.; Stapelfeldt, H.; de Miranda, B. C.; Guillemin, R.; Ismail, I.; Journel, L.; Marchenko, T.; Palaudoux, J.; Penent, F.; Piancastelli, M. N.; Simon, M.; Travnikova, O.; Brausse, F.; Goldsztejn, G.; Rouzée, A.; Géléoc, M.; Geneaux, R.; Ruchon, T.; Underwood, J.; Holland, D. M. P.; Mereshchenko, A. S.; Olshin, P. K.; Johnsson, P.; Maclot, S.; Lahl, J.; Rudenko, A.; Ziaee, F.; Brouard, M.; Rolles, D. Coulomb-Explosion Imaging of Concurrent CH2BrI Photodissociation Dynamics. *Phys. Rev. A* **2017**, *96* (4), 043415. https://doi.org/10.1103/PhysRevA.96.043415.

(11)   Amini, K.; Boll, R.; Lauer, A.; Burt, M.; Lee, J. W. L.; Christensen, L.; Brauße, F.; Mullins, T.; Savelyev, E.; Ablikim, U.; Berrah, N.; Bomme, C.; Düsterer, S.; Erk, B.; Höppner, H.; Johnsson, P.; Kierspel, T.; Krecinic, F.; Küpper, J.; Müller, M.; Müller, E.; Redlin, H.; Rouzée, A.; Schirmel, N.; Thøgersen, J.; Techert, S.; Toleikis, S.; Treusch, R.; Trippel, S.; Ulmer, A.; Wiese, J.; Vallance, C.; Rudenko, A.; Stapelfeldt, H.; Brouard, M.; Rolles, D. Alignment, Orientation, and Coulomb Explosion of Difluoroiodobenzene Studied with the Pixel Imaging Mass Spectrometry (PImMS) Camera. *J. Chem. Phys.* **2017**, *147* (1), 013933. https://doi.org/10.1063/1.4982220.

(12)   Burt, M.; Amini, K.; Lee, J. W. L.; Christiansen, L.; Johansen, R. R.; Kobayashi, Y.; Pickering, J. D.; Vallance, C.; Brouard, M.; Stapelfeldt, H. Communication: Gas-Phase Structural Isomer Identification by Coulomb Explosion of Aligned Molecules. *J. Chem. Phys.* **2018**, *148* (9), 091102. https://doi.org/10.1063/1.5023441.

(13)   Allum, F.; Burt, M.; Amini, K.; Boll, R.; Köckert, H.; Olshin, P. K.; Bari, S.; Bomme, C.; Brauße, F.; Cunha de Miranda, B.; Düsterer, S.; Erk, B.; Géléoc, M.; Geneaux, R.; Gentleman, A. S.; Goldsztejn, G.; Guillemin, R.; Holland, D. M. P.; Ismail, I.; Johnsson, P.; Journel, L.; Küpper, J.; Lahl, J.; Lee, J. W. L.; Maclot, S.; Mackenzie, S. R.; Manschwetus, B.; Mereshchenko, A. S.; Mason, R.; Palaudoux, J.; Piancastelli, M. N.; Penent, F.; Rompotis, D.; Rouzée, A.; Ruchon, T.; Rudenko, A.; Savelyev, E.; Simon, M.; Schirmel, N.; Stapelfeldt, H.; Techert, S.; Travnikova, O.; Trippel, S.; Underwood, J. G.; Vallance, C.; Wiese, J.; Ziaee, F.; Brouard, M.; Marchenko, T.; Rolles, D. Coulomb Explosion Imaging of CH3I and CH2ClI Photodissociation Dynamics. *J. Chem. Phys.* **2018**, *149* (20), 204313. https://doi.org/10.1063/1.5041381.

(14)   Lee, S. K.; Cudry, F.; Lin, Y. F.; Lingenfelter, S.; Winney, A. H.; Fan, L.; Li, W. Coincidence Ion Imaging with a Fast Frame Camera. *Rev. Sci. Instrum.* **2014**, *85* (12), 123303. https://doi.org/10.1063/1.4903856.

(15)   Weeraratna, C.; Amarasinghe, C.; Lee, S. K.; Li, W.; Suits, A. G. Demonstration of Multi-Hit and Multi-Mass Capability of 3D Imaging in a Conventional Velocity Map Imaging Experiment. *J. Chem. Phys.* **2018**, *149* (8), 084202. https://doi.org/10.1063/1.5040589.

(16)   Manidhar, D. M.; Uma Maheswara Rao, K.; Suresh Reddy, C.; Syamasunder, Ch.; Adeppa, K.; Misra, K. An Improved Method for the Preparation of Alkyl/Arylurea Derivatives Using Chlorocarbonylsulfenyl Chloride as Carbonylating Agent. *Res. Chem. Intermed.* **2012**, *38* (9), 2479–2489. https://doi.org/10.1007/s11164-012-0563-4.

(17)   Obreza, A.; Grabrijan, K.; Kadić, S.; Garrido, F. J. de L.; Sosič, I.; Gobec, S.; Jukič, M. Chlorocarbonylsulfenyl Chloride Cyclizations towards Piperidin-3-Yl-Oxathiazol-2-Ones as Potential Covalent Inhibitors of Threonine Proteases. *Acta Chim. Slov.* **2017**, *64* (4), 771–781. https://doi.org/10.17344/acsi.2017.3883.

(18)   Izawa, S.; Nakatsuji, H.; Tanabe, Y. Straightforward Synthesis of *N*-Methyl-4-(Pin)B-2(3*H*)-Benzothiazol-2-One: A Promising Cross-Coupling Reagent. *Molbank* **2018**, *2018* (1), M976. https://doi.org/10.3390/M976.

(19)   Shen, Q.; Hagen, K. Molecular Structure and Conformation of Gaseous Chlorocarbonylsulfenyl Chloride, ClSCOCl, as Determined by Electron Diffraction. *J. Mol. Struct.* **1985**, *128* (1), 41–48. https://doi.org/10.1016/0022-2860(85)85039-0.

(20)   Jubert, A. H.; Della Védova, C. O.; Aymonino, P. J. Theoretical Calculation of the Rotational Barrier, Valence Force Constants and Experimental Electronic Spectrum of Chlorocarbonylsulphenyl Chloride (ClC(O)SCl). *Croat. Chem. Acta* **1987**, *60* (2), 207–213.

(21) Mack, H. G.; Oberhammer, H.; Della Vedova, C. O. Conformational Properties and Gas-Phase Structure of (Fluorocarbonyl)Sulfenyl Chloride, FC(O)SCl; Electron Diffraction, Vibrational Analysis, and Ab Initio Calculations. *J. Phys. Chem.* **1991**, *95* (11), 4238–4241. https://doi.org/10.1021/j100164a014.

(22) Romano, R. M.; Della Védova, C. O.; Downs, A. J.; Greene, T. M. Matrix Photochemistry of Syn-(Chlorocarbonyl)Sulfenyl Bromide, Syn-ClC(O)SBr: Precursor to the Novel Species Anti-ClC(O)SBr, Syn-BrC(O)SCl, and BrSCl. *J. Am. Chem. Soc.* **2001**, *123* (24), 5794–5801. https://doi.org/10.1021/ja010252f.

(23) Erben, M. F.; Della Védova, C. O.; Romano, R. M.; Boese, R.; Oberhammer, H.; Willner, H.; Sala, O. Anomeric and Mesomeric Effects in Methoxycarbonylsulfenyl Chloride, CH3OC(O)SCl: An Experimental and Theoretical Study. *Inorg. Chem.* **2002**, *41* (5), 1064–1071. https://doi.org/10.1021/ic010748y.

(24) Romano, R. M.; Védova, C. O. D.; Downs, A. J.; Parsons, S.; Smith, C. Structural and Vibrational Properties of ClC(O)SY Compounds with Y = Cl and CH3. *New J. Chem.* **2003**, *27* (3), 514–519. https://doi.org/10.1039/B209005H.

(25) Romano, R. M.; Della Védova, C. O.; Downs, A. J. Matrix Photochemistry of the Chlorocarbonyl Sulfenyl Compounds ClC(O)SY, with Y = Cl or CH3. *J. Phys. Chem. A* **2004**, *108* (35), 7179–7187. https://doi.org/10.1021/jp048756y.

(26) Erben, M. F.; Romano, R. M.; Della Védova, C. O. Ionic Fragmentation on ClC(O)SCl. Evidence of a Highly Charged Molecular Ion and Confirmation of Unusual Dissociation Mechanisms for Halocarbonylsulfenyl Chlorides. *J. Phys. Chem. A* **2005**, *109* (2), 304–313. https://doi.org/10.1021/jp045732i.

(27) Lin, L.; Ding, W.-J.; Fang, W.-H.; Liu, R.-Z. Insights into the Photochemical Processes of ClC(O)SCl from Ab Initio Calculations. *J. Phys. Chem. A* **2006**, *110* (28), 8744–8749. https://doi.org/10.1021/jp054497g.

(28) Geronés, M.; Erben, M. F.; Romano, R. M.; Della Védova, C. O.; Yao, L.; Ge, M. He I Photoelectron Spectra and Valence Synchrotron Photoionization for XC(O)SCl (X = F, Cl) Compounds. *J. Phys. Chem. A* **2008**, *112* (11), 2228–2234. https://doi.org/10.1021/jp7101034.

(29) Proch, D.; Trickl, T. A High-intensity Multi-purpose Piezoelectric Pulsed Molecular Beam Source. *Rev. Sci. Instrum.* **1989**, *60* (4), 713–716. https://doi.org/10.1063/1.1141006.

(30) Townsend, D.; Minitti, M. P.; Suits, A. G. Direct Current Slice Imaging. *Rev. Sci. Instrum.* **2003**, *74* (4), 2530–2539. https://doi.org/10.1063/1.1544053.

(31) Hohenberg, P.; Kohn, W. Inhomogeneous Electron Gas. *Phys. Rev.* **1964**, *136* (3B), B864–B871.

(32) Kohn, W.; Sham, L. J. Self-Consistent Equations Including Exchange and Correlation Effects. *Phys. Rev.* **1965**, *140* (4A), A1133–A1138.

(33) Chai, J.-D.; Head-Gordon, M. Long-Range Corrected Hybrid Density Functionals with Damped Atom–Atom Dispersion Corrections. *Phys. Chem. Chem. Phys.* **2008**, *10* (44), 6615–6620. https://doi.org/10.1039/B810189B.

(34) Dunning Jr., T. H. Gaussian Basis Sets for Use in Correlated Molecular Calculations. I. The Atoms Boron through Neon and Hydrogen. *J. Chem. Phys.* **1989**, *90* (2), 1007–1023. https://doi.org/10.1063/1.456153.

(35) Kendall, R. A.; Dunning Jr., T. H.; Harrison, R. J. Electron Affinities of the First-row Atoms Revisited. Systematic Basis Sets and Wave Functions. *J. Chem. Phys.* **1992**, *96* (9), 6796–6806. https://doi.org/10.1063/1.462569.

(36) Woon, D. E.; Dunning Jr., T. H. Gaussian Basis Sets for Use in Correlated Molecular Calculations. III. The Atoms Aluminum through Argon. *J. Chem. Phys.* **1993**, *98* (2), 1358–1371. https://doi.org/10.1063/1.464303.

(37) Bauernschmitt, R.; Ahlrichs, R. Treatment of Electronic Excitations within the Adiabatic Approximation of Time Dependent Density Functional Theory. *Chem. Phys. Lett.* **1996**, *256* (4), 454–464. https://doi.org/10.1016/0009-2614(96)00440-X.

(38) Casida, M. E.; Jamorski, C.; Casida, K. C.; Salahub, D. R. Molecular Excitation Energies to High-Lying Bound States from Time-Dependent Density-Functional Response Theory: Characterization and Correction of the Time-Dependent Local Density Approximation Ionization Threshold. *J. Chem. Phys.* **1998**, *108* (11), 4439–4449. https://doi.org/10.1063/1.475855.

(39) Stratmann, R. E.; Scuseria, G. E.; Frisch, M. J. An Efficient Implementation of Time-Dependent Density-Functional Theory for the Calculation of Excitation Energies of Large Molecules. *J. Chem. Phys.* **1998**, *109* (19), 8218–8224. https://doi.org/10.1063/1.477483.

(40) Van Caillie, C.; Amos, R. D. Geometric Derivatives of Excitation Energies Using SCF and DFT. *Chem. Phys. Lett.* **1999**, *308* (3), 249–255. https://doi.org/10.1016/S0009-2614(99)00646-6.

(41) Van Caillie, C.; Amos, R. D. Geometric Derivatives of Density Functional Theory Excitation Energies Using Gradient-Corrected Functionals. *Chem. Phys. Lett.* **2000**, *317* (1), 159–164. https://doi.org/10.1016/S0009-2614(99)01346-9.

(42) Furche, F.; Ahlrichs, R. Adiabatic Time-Dependent Density Functional Methods for Excited State Properties. *J. Chem. Phys.* **2002**, *117* (16), 7433–7447. https://doi.org/doi:http://dx.doi.org/10.1063/1.1508368.

(43) Scalmani, G.; Frisch, M. J.; Mennucci, B.; Tomasi, J.; Cammi, R.; Barone, V. Geometries and Properties of Excited States in the Gas Phase and in Solution: Theory and Application of a Time-Dependent Density Functional Theory Polarizable Continuum Model. *J. Chem. Phys.* **2006**, *124* (9), 094107. https://doi.org/10.1063/1.2173258.

(44) Frisch, M. J.; Trucks, G. W.; Schlegel, H. B.; Scuseria, G. E.; Robb, M. A.; Cheeseman, J. R.; Scalmani, G.; Barone, V.; Mennucci, B.; Petersson, G. A.; Nakatsuji, H.; Caricato, M.; Li, X.; Hratchian, H. P.; Izmaylov, A. F.; Bloino, J.; Zheng, G.; Sonnenberg, J. L.; Hada, M.; Ehara, M.; Toyota, K.; Fukuda, R.; Hasegawa, J.; Ishida, M.; Nakajima, T.; Honda, Y.; Kitao, O.; Nakai, H.; Vreven, T.; Montgomery, Jr., J. A.; Peralta, J. E.; Ogliaro, F.; Bearpark, M.; Heyd, J. J.; Brothers, E.; Kudin, K. N.; Staroverov, V. N.; Keith, T.; Kobayashi, R.; Normand, J.; Raghavachari, K.; Rendell, A.; Burant, J. C.; Iyengar, S. S.; Tomasi, J.; Cossi, M.; Rega, N.; Millam, J. M.; Klene, M.; Knox, J. E.; Cross, J. B.; Bakken, V.; Adamo, C.; Jaramillo, J.; Gomperts, R.; Stratmann, R. E.; Yazyev, O.; Austin, A. J.; Cammi, R.; Pomelli, C.; Ochterski, J. W.; Martin, R. L.; Morokuma, K.; Zakrzewski, V. G.; Voth, G. A.; Salvador, P.; Dannenberg, J. J.; Dapprich, S.; Daniels, A. D.; Farkas, O.; Foresman, J. B.; Ortiz, J. V.; Cioslowski, J.; Fox, D. J. *Gaussian 09*; Gaussian, Inc.: Wallingford CT, 2013.

(45) Thompson, J. O. F.; Amarasinghe, C.; Foley, C. D.; Suits, A. G. Finite Slice Analysis (FINA)—A General Reconstruction Method for Velocity Mapped and Time-Sliced Ion Imaging. *J. Chem. Phys.* **2017**, *147* (1), 013913. https://doi.org/10.1063/1.4979305.

(46) Thompson, J. O. F.; Amarasinghe, C.; Foley, C. D.; Rombes, N.; Gao, Z.; Vogels, S. N.; van de Meerakker, S. Y. T.; Suits, A. G. Finite Slice Analysis (FINA) of Sliced and Velocity

Mapped Images on a Cartesian Grid. *J. Chem. Phys.* **2017**, *147* (7), 074201. https://doi.org/10.1063/1.4986966.

(47) Frasinski, L. J.; Codling, K.; Hatherly, P.; Barr, J.; Ross, I. N.; Toner, W. T. Femtosecond Dynamics of Multielectron Dissociative Ionization by Use of a Picosecond Laser. *Phys. Rev. Lett.* **1987**, *58* (23), 2424–2427. https://doi.org/10.1103/PhysRevLett.58.2424.

(48) Cornaggia, C.; Schmidt, M.; Normand, D. Coulomb Explosion of CO_2 in an Intense Femtosecond Laser Field. *J. Phys. B At. Mol. Opt. Phys.* **1994**, *27* (7), L123–L130. https://doi.org/10.1088/0953-4075/27/7/002.

(49) Hering, Ph.; Cornaggia, C. Coulomb Explosion of N_{2} and CO_{2} Using Linearly and Circularly Polarized Femtosecond Laser Pulses. *Phys. Rev. A* **1999**, *59* (4), 2836–2843. https://doi.org/10.1103/PhysRevA.59.2836.

(50) Brewczyk, M.; Frasinski, L. J. Thomas-Fermi-Dirac Model of Nitrogen Molecules Ionized by Strong Laser Fields. *J. Phys. B At. Mol. Opt. Phys.* **1991**, *24* (13), L307–L313. https://doi.org/10.1088/0953-4075/24/13/002.

(51) Posthumus, J. H.; Giles, A. J.; Thompson, M. R.; Shaikh, W.; Langley, A. J.; Frasinski, L. J.; Codling, K. The Dissociation Dynamics of Diatomic Molecules in Intense Laser Fields. *J. Phys. B At. Mol. Opt. Phys.* **1996**, *29* (14), L525–L531. https://doi.org/10.1088/0953-4075/29/14/004.

TABLE OF CONTENTS GRAPHIC